



Bioinspired hollow and hierarchically porous MO_x ($\text{M} = \text{Ti}, \text{Si}$)/carbon microellipsoids supported with Fe_2O_3 for heterogenous photochemical oxidation

Lei Qin^a, Minmin Liu^a, Yujiao Wu^a, Zehai Xu^a, Xinwen Guo^b, Guoliang Zhang^{a,*}

^a Institute of Oceanic and Environmental Chemical Engineering, State Key Lab Breeding Base of Green Chemical Synthesis Technology, Zhejiang University of Technology, Hangzhou 310014, China

^b State Key Laboratory of Fine Chemicals, Department of Catalysis Chemistry and Engineering, Dalian University of Technology, Dalian 116012, China

ARTICLE INFO

Article history:

Received 5 February 2016

Received in revised form 19 April 2016

Accepted 25 April 2016

Available online 27 April 2016

Keywords:

MO_x ($\text{M} = \text{Ti}, \text{Si}$)/carbon microellipsoids

Biotemplating

Surface sol-gel coating

Fe_2O_3 nanoparticles

Photochemical oxidation

ABSTRACT

Porous carbon materials as a class of highly promising functional materials have attracted widespread interests. However, rational design and synthesis of carbon supported catalysts for long-term use still remains a big challenge. Herein, a facile surface sol-gel coating method via biotemplating technique was first employed to prepare hollow and hierarchically porous MO_x ($\text{M} = \text{Ti}, \text{Si}$)/carbon microellipsoids with immobilized Fe_2O_3 NPs in pores. The easily-reached and carbon-rich pollen was chosen to play double roles as both template and carbon source. The obtained natural carbon materials acted as trapping centers for photo-induced electrons and effectively improved visible-light photocatalytic activity and stability. By using this method, we can not only fabricate very active and reusable heterogenous catalysts without any additional surfactants, but also obviously reduce the fabrication time, dosage of chemicals and thickness of inorganic colloids. Since the bioinspired structure can provide high surface area and multiple pore size distribution for NPs to homogeneously disperse on the wall of carbon-based composites, the approach can be applied more generally to various biomaterials.

© 2016 Elsevier B.V. All rights reserved.

Abbreviations: AC, active carbon; BET, Brunauer Emmett and Teller; EDS, energy dispersive spectroscopy; ESI[†], Electronic Supplementary Information; Fe_2O_3 @ pollen carbon, pollens calcined for 4 h and supported with Fe_2O_3 by hydrothermal process; Fe_2O_3 @ MO_x /C-473, Fe_2O_3 @ MO_x /C-673 and Fe_2O_3 @ MO_x /C-873 ($\text{M} = \text{Ti}$ and Si) MO_x /C-473 MO_x /C-673 and MO_x /C-873 ($\text{M} = \text{Ti}$ and Si) supported with Fe_2O_3 by hydrothermal process; Fe_2O_3 @pollen, pollens supported with Fe_2O_3 by hydrothermal process; Fe_2O_3 @pollen-473, Fe_2O_3 @pollen-673 and Fe_2O_3 @pollen-873, pollens calcined at 473 673 and 873 K and supported with Fe_2O_3 by hydrothermal process; FTIR, Fourier transform infrared spectrophotometers; HRSEM, high resolution scanning electron microscope; HRTEM, high resolution transmission electron microscopy; ICP, inductive coupled plasma emission spectrometer; MO_x ($\text{M} = \text{Ti}$ and Si) /C, MO_x ($\text{M} = \text{Ti}$ and Si)/pollens calcined for 4 h; MO_x /C-473, MO_x /C-673 and MO_x /C-873 ($\text{M} = \text{Ti}$ and Si), MO_x ($\text{M} = \text{Ti}$ and Si)/pollens calcined at 473 673 and 873 K for 4 h; NPs, nanoparticles; SEM, scanning electron microscope; SiO_x /pollen, silicon-coated pollen grains; TEM, transmission electron microscopy; TG, thermogravimetric; TiO_x /pollen, titanium-coated pollen grains; XPS, X-ray photoelectron spectroscopy; XRD, X-ray diffraction; Zn-Al-MMO, porous mixed metal oxides.

* Corresponding author.

E-mail address: guoliangz@zjut.edu.cn (G. Zhang).

1. Introduction

Porous carbon materials as a class of highly promising functional materials have attracted widespread interests in the field of adsorption, separation, gas storage, fuel cells and catalysis due to their good electronic conductivity, high availability, large surface area and porosity, and low cost [1]. Over the past decades, more attention has been laid on supporting noble-metal, metal oxide nanoparticles (NPs) and semiconductor quantum dots on carbon materials for various heterogeneous catalytic reactions [2–4]. However, rational design and synthesis of carbon supported catalysts for long-term use still remains a big challenge.

Since a variety of inorganic compounds including TiO_2 , ZnO and SiO_2 have been tried to combine with carbon to endow more hybrid surface properties than carbon alone, such as excellent mechanical, electrical, chemical and optical properties [5–7], it can be imaginable that carbon-inorganic composites as the support may possess valuable characters in the catalytic oxidation, compared with pure carbon or inorganic compounds. Moreover, because the catalytic activity of carbon-based materials is closely associated with the morphology and microstructure, many efforts have been made to develop different composites with multiple structures [8]. Among

them, the hierarchically porous and hollow structure with large surface area and shell permeability are drawing significant attention, which plays an important role in the diffusion of guest species and active sites through an inorganic network of pores and channels [9,10]. Therefore, it is essential for developing a general and facile method to fabricate advanced carbon-inorganic composites with both multiple functions and controlled structure.

Although the soft/hard templating technique and water-in-oil (W/O) emulsion method are often used to prepare the hollow or hierarchically porous composites [11,12], the expensive chemical surfactants, complex steps and long time are required in the fabrication processes. Compared with these methods, biotemplating technique provides an impressive platform to facilitate achieve morphology-controllable materials with anticipated structural specialty, complexity, and relevant unique properties and there is no need for any additional surfactants in the preparation process [13]. Inspired by the inexpensive, abundant, environmentally benign, and renewable characters offered by nature, some useful biological resources such as cotton fibers, bamboo, butterfly wings and viruses have been applied to synthesize the hybrid inorganic materials with multiple scales and hierarchical structure for the application of Li-ion batteries, photonic crystals and dye-sensitized solar cells [14,15]. In recent years, porous mixed metal oxides (Zn-Al-MMO) and inorganic materials such as CdS were also fabricated through biomaterial templating which exhibited excellent catalytic performance due to the unique biological structures [16,17]. To our knowledge, few studies on preparation of carbon-inorganic composites supported with active sites for heterogeneous catalysis by biotemplating technique have been reported so far.

Herein, we report a facile surface sol-gel coating method for fabricating hollow and hierarchically porous MO_x ($M = \text{Ti}, \text{Si}$)/carbon composites with immobilized Fe_2O_3 NPs in pores via biotemplating technique. Our approach can be applied more generally to various biomaterials, but we demonstrate our key findings here with the example of pollen since the compositional and nano/microstructural design of pollen grains markedly differs from that of common materials, which are always considered as a kind of core-shell material. The core is easy to decompose when exposing to the environment, but the shell is composed of specific hierarchical scaffolds [18–21]. Moreover, the tough outer exine exhibits a series of complex surface features in microscale and is resistant to heat and common solvents, which makes it possible for a wide range of carbon-inorganic composites. To study this concept, we choose the easily-reached and carbon-rich lily pollen to play dual roles as both the template and the carbon source. The obtained natural carbon materials may act as trapping centers for photo-induced electrons and are applied to improve visible-light photocatalytic activity and stability. We also go forward to explore how the complex of pollen structure and strong interaction between carbon and inorganic compound can promote catalytic function of the composites.

As evidenced in Scheme 1, tetrabutyl titanate (TBT) and tetraethyl orthosilicate (TEOS) were uniformly coated on the outer and inner layer of exine, and in-situ hydrolysis occurred to sol-gel on the interface of cell by sparging the droplet. Compared with traditional replicated approach, our strategy can obviously reduce the fabrication time, dosage of chemicals and thickness of inorganic colloids. In order to explore the relationship between structure/properties of carbon-based composite and activity, we prepared porous MO_x/C , hollow porous MO_x/C , and hollow porous MO_2 ($M = \text{Ti}, \text{Si}$) by varying calcination temperature. During the heat treatment in air, the carbonaceous organic compounds arising from pollen were broken down. Finally, in situ grown Fe_2O_3 was well-dispersed into the composite microellipsoids after hydrothermal treatment. Compared with traditional materials such as active carbon, P25 and SiO_2 , the pollen-templated

carbon-based microellipsoids supported with Fe_2O_3 exhibited much higher photo-oxidation activity, owing to the multiple structure and unique properties of bioinspired carbon-inorganic composites.

2. Experimental section

2.1. Materials

Tetraethyl orthosilicate, tetrabutyl titanate, acetylacetone, ferric nitrate, hydrochloric acid (HCl, 35 wt.%, AR) and alcohol ($\text{C}_2\text{H}_5\text{OH}$, AR) were purchased from Sinopharm chemical Reagent Co., Ltd. (China). Deionized water was made by RO-EDI system with cations and the anions were measured by an IRIS Intrepid ICP and a Metrohm 861 Compact IC. The lily pollen grains were collected from the local garden.

2.2. Preparation of various catalysts

2.2.1. Preparation of pollen grains

Firstly, the pollen grains were cleaned by immersion in a mixture of methanol and deionized water (3:1, v/v) for several hours and dried under vacuum at 373 K. Secondly, the as-cleaned pollens were immersed in 0.5 M of hydrochloric acid to remove surface inorganic impurities followed by rinsing with deionized water and drying by vacuum. The deionized water used was made by RO-EDI equipment in which the ionic concentration was monitored by IRIS Intrepid ICP and Metrohm 861 Compact IC to meet the requirement of $\sigma \leq 0.5 \mu\text{S cm}^{-1}$.

2.2.2. Synthesis of TiO_x/C replicas

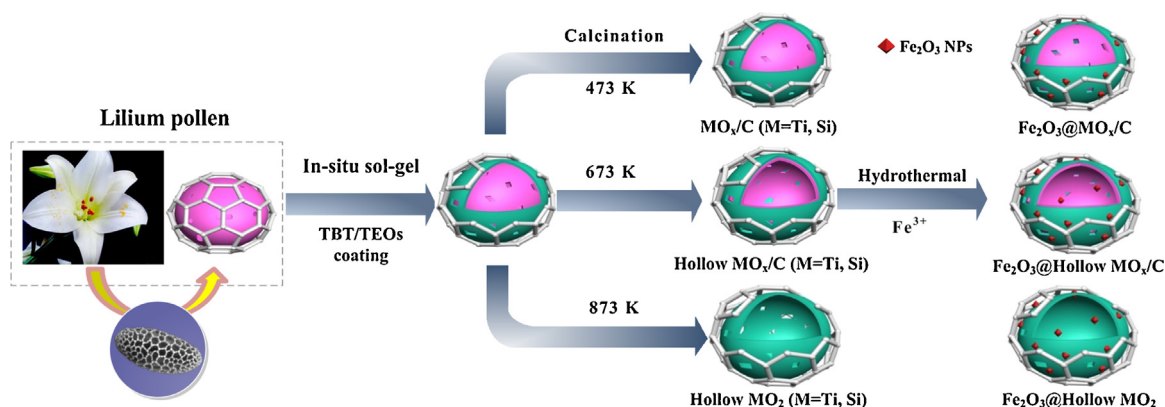
In a typical synthesis, 1.0 g of pollen grains were added into the 50 ml mixture of tetrabutyl titanate and acetylacetone, and then stirred in the flowing nitrogen atmosphere for 10 h. The precipitates were filtered and washed with alcohol to remove undesirable materials. The as-prepared pollen grains were dried in an oven. The above process was repeated for several times. After coating, the products were transferred into a glass tube, and then the droplets of alcohol and water (1:1, v/v) were sparged on it with repeated shaking and rotation of the tube in order to ensure homogeneous hydrolysis. Afterwards, the mixture was stirred at 333 K in an oil bath for 30 min. Finally, the obtained titanium-coated pollen grains were filtered, cleaned with distilled deionized water, and then dried in a vacuum. In order to obtain the resulting composites with different structures and properties, the as-synthesized samples ($\text{TiO}_x/\text{pollen}$) were treated in a stream of air at 473, 673 and 873 K for 4 h, which were denoted as $\text{TiO}_x/\text{C-473}$, $\text{TiO}_x/\text{C-673}$ and $\text{TiO}_x/\text{C-873}$, respectively.

2.2.3. Synthesis of SiO_x/C replicas

Typically, 1.0 g of pollen grains was added into 10 ml of tetraethoxysilane in a beaker under strong stirring for 18 h. Then the mixture was filtered and immersed in alcohol for a while. Further procedures were similar to the synthesis of TiO_x/C replicas. The resulting samples ($\text{SiO}_x/\text{pollen}$) were labelled as $\text{SiO}_x/\text{C-473}$, $\text{SiO}_x/\text{C-673}$ and $\text{SiO}_x/\text{C-873}$, respectively.

2.2.4. Synthesis of $\text{Fe}_2\text{O}_3@ \text{TiO}_x/\text{C}$ replicas

The 0.5 g as-prepared TiO_x/C replicas ($\text{TiO}_x/\text{C-473}$, $\text{TiO}_x/\text{C-673}$, $\text{TiO}_x/\text{C-873}$) were dispersed in a 30 ml ethanol/water mixture (1:1, v/v) containing the Fe^{3+} ions (metal ion/support = 10%, w/w). The mixture was stirred at room temperature to form a homogeneous solution, and then transferred into the 50 ml of Teflon-lined stainless-steel autoclave and heated at 333 K for 8 h. Finally, the obtained powders were cleaned with distilled water and dried in a



Scheme 1. Fabrication of different complex inorganic micron-sized ellipsoids supported with Fe_2O_3 by surface in situ sol-gel replication of pollen grains.

vacuum. The resulting samples were labelled as $\text{Fe}_2\text{O}_3@\text{TiO}_x/\text{C}$ -473, $\text{Fe}_2\text{O}_3@\text{TiO}_x/\text{C}$ -673 and $\text{Fe}_2\text{O}_3@\text{TiO}_x/\text{C}$ -873, respectively.

2.2.5. Synthesis of $\text{Fe}_2\text{O}_3@\text{SiO}_x/\text{C}$ replicas

The pathway used to fabricate $\text{Fe}_2\text{O}_3@\text{SiO}_x/\text{C}$ replicas was similar to the synthesis of $\text{Fe}_2\text{O}_3@\text{TiO}_x/\text{C}$ replicas, which were denoted as $\text{Fe}_2\text{O}_3@\text{SiO}_x/\text{C}$ -473, $\text{Fe}_2\text{O}_3@\text{SiO}_x/\text{C}$ -673 and $\text{Fe}_2\text{O}_3@\text{SiO}_x/\text{C}$ -873, respectively.

2.2.6. Synthesis of $\text{Fe}_2\text{O}_3@\text{pollen carbon}$

The pre-treated pollen grains were firstly calcined at 473, 673 and 873 K in nitrogen atmosphere, respectively. The as-synthesized pollens decorated with Fe^{3+} ions (metal ion/support = 10%, w/w) were then prepared similar to the synthesis of $\text{Fe}_2\text{O}_3@\text{TiO}_x/\text{C}$ replicas. Finally, the resulting products were washed and dried in a vacuum, which were abbreviated as $\text{Fe}_2\text{O}_3@\text{pollen}$ -473, $\text{Fe}_2\text{O}_3@\text{pollen}$ -673 and $\text{Fe}_2\text{O}_3@\text{pollen}$ -873, respectively.

2.2.7. Synthesis of $\text{Fe}_2\text{O}_3@\text{pollen}$, $\text{Fe}_2\text{O}_3@\text{AC}$, $\text{Fe}_2\text{O}_3@\text{P25}$ and $\text{Fe}_2\text{O}_3@\text{SiO}_2$

The pre-treated pollen grains, activated carbon, P25, and SiO_2 were decorated with Fe^{3+} ions (metal ion/support = 10%, w/w) by hydrothermal process similar to the synthesis of $\text{Fe}_2\text{O}_3@\text{TiO}_x/\text{C}$ replicas.

2.3. Characterization of catalysts

Surface morphology and structure of the synthesized samples were observed by using the Hitachi JEM-1200EX transmission electron microscopy (Hitachi, Japan) and JEM-2100 transmission electron microscopy (Jeol, Japan) and Tecnai G2 F30 S-Twin high resolution transmission electron microscopy (Philips-FEI, Holland). Energy dispersive spectroscopy (Hitachi, S-3700N, Japan) and Inductive coupled plasma emission spectrometer (ICP) were taken for the composition and concentration analysis of all the samples. Fourier transform infrared (FTIR) of the samples was tested by the KBr disk technique on the Nicolet 6700 spectrometer (Thermo, USA). An ASAP 2020 surface area and porosity analyzer (Micromeritics, USA) was employed to analyze the nitrogen adsorption–desorption isotherms and specific surface areas of prepared samples. X-ray photoelectron spectroscopy (XPS) measurement of samples was carried out on a RBD upgraded PHI-5000C ESCA system (Perkin Elmer) with Mg K α radiation ($h\nu = 1253.6\text{ eV}$), and the contaminant carbon (C1s = 284.6 eV) was used to calibrate the binding energies of others elements. X'Pert PRO X-ray diffractometer (PANalytical, Cu K α radiation) was used to determine the X-ray diffraction (XRD) of the nanocomposites. Thermogravimetric (TG) analysis was

performed on TQ5000IR Analyzer under a condition of heating rate at 5 °C/min in air.

2.4. Catalytic experiments

The photocatalytic oxidation experiments were performed in a cylindrical Pyrex vessel. A 200 W halogen lamp (purchased from Beijing Lighting Research Institute) was positioned at the top of the vessel. A given concentration of catalyst powder (0.2 g/L) was placed in 50 ml mixture containing water and reactive brilliant red X-3B dye (100 mg/L). The initial pH value of solution was adjusted to the nearly neutral value (pH = 5.0). Prior to reaction, in order to establish the adsorption/desorption equilibrium, the suspension was sonicated and oscillated in the darkness for 30 min. Catalytic oxidation reaction started after adding a certain concentration of H_2O_2 (9.8 mmol/L) to the solution with the lamp turning on. In the experiment, all glass vessels were kept at 303 K in a thermostatic water bath oscillator.

3. Results and discussion

3.1. Catalysts characterization

The native pollen grains used in this work were of typical 40–50 μm in length and showed a characteristic ellipsoidal morphology (Fig. 1a). The wall of shell was actually composed of regular hexagon-shaped frameworks and porous epidermis. The pore of polygonous networks on the exine of pollen grains was with a diameter of 5–10 μm . Such open macropore networks and well-defined micrometer-sized channels can greatly improve the accessibility of surface. The experimental result clearly depicts that $\text{TiO}_x/\text{pollen}$ and $\text{SiO}_x/\text{pollen}$ replicate the nanoscale topography of surface features (including the hexagon frameworks) and size of cells (Fig. 1b and c), and energy-dispersive spectroscopy (EDS) elemental mapping indicates that the distribution of Ti and Si elements was homogeneous on the external surface of pollen structure (Fig. 1f) (more details of EDS measurement on Fig. S1 ESI†). It confirms the surface sol-gel coating method as high-resolution replication procedure. Moreover, as illustrated by HRSEM images (Fig. 1d and e), the porous network of the exine of pollen grain and its hollow structure can be observed after the pre-treatment process.

Fig. 2 shows representative SEM images of different supported composite microellipsoids. For original pollen grains, it was found that the collapse of frameworks happened when the calcination temperature was higher than 673 K (Fig. 2c). However, the ellipsoidal structure of $\text{MO}_x/\text{pollen}$ can still be well kept during thermal treatment, which indicated that the incorporation of inorganic species could enhance the thermal-stability of carbon structure.

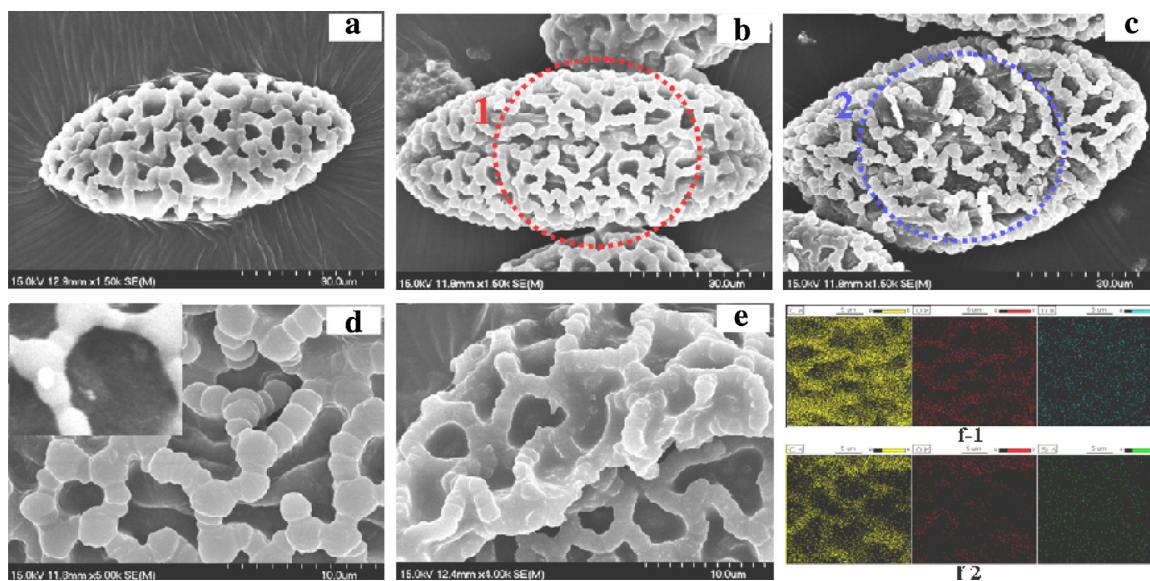


Fig. 1. SEM images of pollen (a), $\text{TiO}_x/\text{pollen}$ (b) and $\text{SiO}_x/\text{pollen}$ (c); HRSEM images of $\text{MO}_x/\text{pollen}$ calcined at 673 K (d, e); and EDS elemental mapping of $\text{TiO}_x/\text{pollen}$ and $\text{SiO}_x/\text{pollen}$ (f).

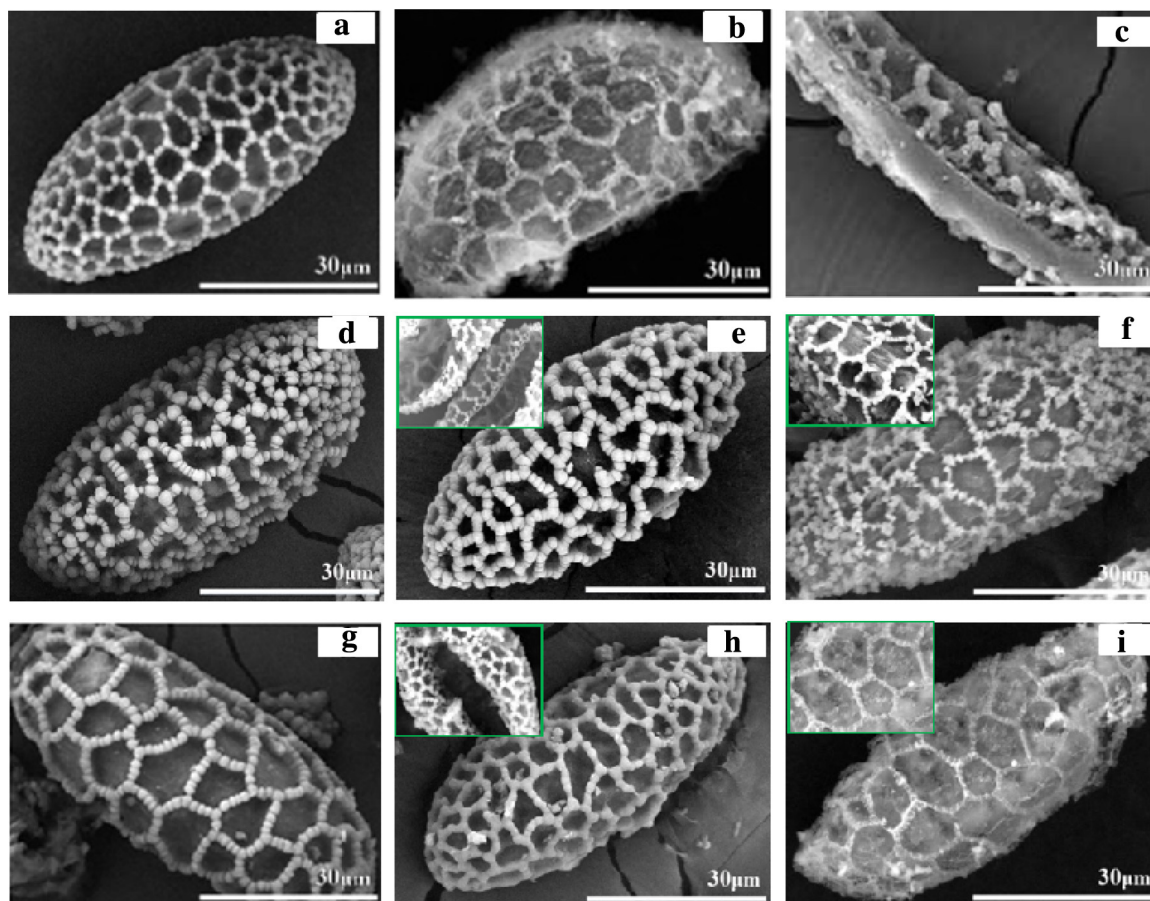


Fig. 2. SEM images of $\text{Fe}_2\text{O}_3/\text{pollen}$ -473 (a), $\text{Fe}_2\text{O}_3/\text{pollen}$ -673 (b), $\text{Fe}_2\text{O}_3/\text{pollen}$ -873 (c), $\text{Fe}_2\text{O}_3/\text{TiO}_x/\text{C}$ -473 (d), $\text{Fe}_2\text{O}_3/\text{TiO}_x/\text{C}$ -673 (e), $\text{Fe}_2\text{O}_3/\text{TiO}_x/\text{C}$ -873 (f), $\text{Fe}_2\text{O}_3/\text{SiO}_x/\text{C}$ -473 (g), $\text{Fe}_2\text{O}_3/\text{SiO}_x/\text{C}$ -673 (h) and $\text{Fe}_2\text{O}_3/\text{SiO}_x/\text{C}$ -873 (i). Insert of (e and h) is SEM images of the hollow structure for composite microellipsoids.

After decorated with Fe_2O_3 , it was clear that the morphology and polygonous network of outer layer remained intact, indicating that this porous ellipsoidal structure can be maintained during the high temperature calcination (Fig. 3). For comparison, the hollow interior feature of $\text{Fe}_2\text{O}_3/\text{MO}_x/\text{C}$ can be observed

(Fig. 2e and h), which was attributed to decomposition of the core substances of pollen after calcined at 673 K. Meanwhile, the features were also presented in the hollow inorganic MO_x replicas (calcined at 873 K), along with the macroporosity due to the removal of biological template [18,19]. By using EDS, the elemental

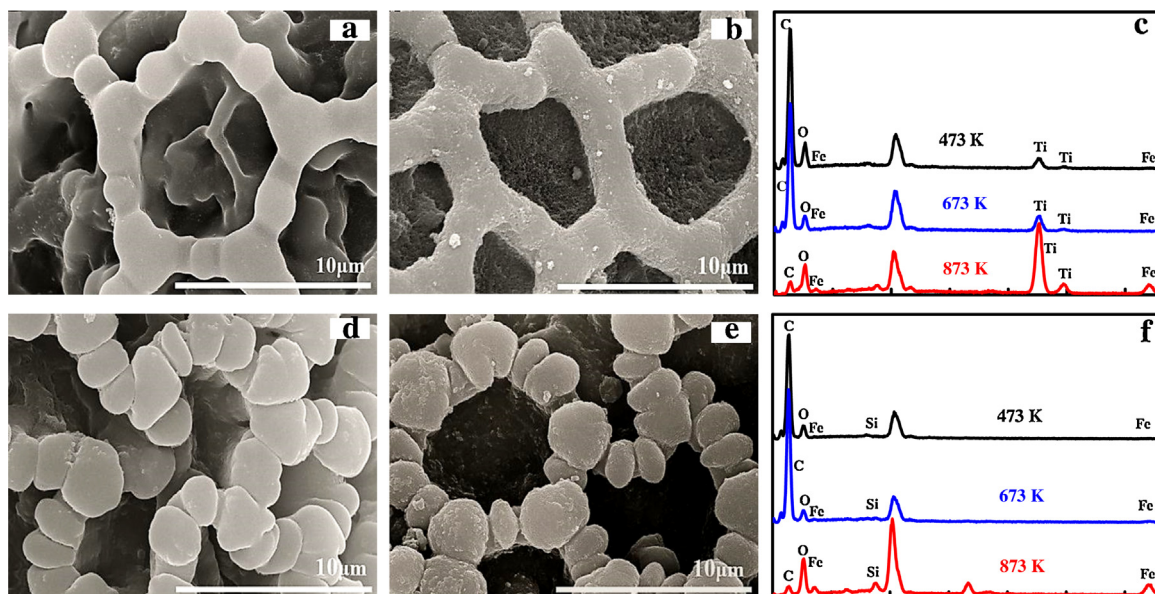


Fig. 3. HRSEM images of hollow porous TiO_x/C -673 (a), $\text{Fe}_2\text{O}_3@\text{TiO}_x/\text{C}$ -673 (b) and EDS of the different $\text{Fe}_2\text{O}_3@\text{TiO}_x/\text{C}$ composites (c); hollow porous SiO_x/C -673 (d), $\text{Fe}_2\text{O}_3@\text{SiO}_x/\text{C}$ -673 (e) and EDS of $\text{Fe}_2\text{O}_3@\text{SiO}_x/\text{C}$ composites (f).

compositions of the composites were examined (Fig. 3c and f). It confirmed that the replicas consisted of Fe, Si, Ti, O and C elements. With the increase of calcination temperature, the mass ratio of Ti and Si obviously increased, but an evident reduction in C content was observed. The loading of Fe for different samples calcined at respective temperatures was shown in Table S1. By comparison, it was found that the supported Fe_2O_3 amount of $\text{Fe}_2\text{O}_3@\text{TiO}_x/\text{C}$ was higher than that of $\text{Fe}_2\text{O}_3@\text{SiO}_x/\text{C}$ samples.

To investigate more details in thermal stability and chemical composition of $\text{TiO}_x/\text{pollen}$ and $\text{SiO}_x/\text{pollen}$ microellipsoids, TG analysis was further made (Fig. S2 ESI[†]). A slight weight loss of all the microellipsoids occurred below 473 K due to the release of physically adsorbed water. The major mass loss for both samples was recorded in the temperature range of 473–673 K, which was attributed to the decomposition of different oxygen functional groups and carbon networks [22]. This well verified that the organic core of pollen was destroyed when calcined at 673 K and the hollow structure appeared. After the temperature rose to 873 K, all carbon in composite microellipsoids was converted to CO_2 . According to the TGA results, the TiO_2 and SiO_2 contents in the $\text{TiO}_x/\text{pollen}$ and $\text{SiO}_x/\text{pollen}$ composite were calculated to be 5.70 and 5.06%, respectively. By analysis, the carbon and organics contents of the $\text{TiO}_x/\text{pollen}$ calcined at 473 and 673 K were 88.30 and 29.93%, while they were 84.71 and 35.28% for sample $\text{SiO}_x/\text{pollen}$ calcined at 473 and 673 K.

According to the N_2 adsorption/desorption isotherms (Fig. 4a), it is found the curve of all the samples display a typical type IV pattern with a hysteresis loop. The hysteresis loop in the low relative (P/P_0) range of 0.4–1.0 may be ascribed to the presence of mesoporous structure. Compared with $\text{Fe}_2\text{O}_3@\text{pollen}$ -673, it is worth to note that the specific surface area of $\text{Fe}_2\text{O}_3@\text{TiO}_x/\text{C}$ -673 and $\text{Fe}_2\text{O}_3@\text{SiO}_x/\text{C}$ -673 obviously increases from 39.5 to 282.3 and 137.3 $\text{m}^2 \text{g}^{-1}$, respectively (Table S2 ESI[†]). Meanwhile, an obvious increase in the pore volume was also observed for these two composites. Due to larger surface area and pore volume, the Fe loading of $\text{Fe}_2\text{O}_3@\text{TiO}_x/\text{C}$ -673 was higher than that of $\text{Fe}_2\text{O}_3@\text{SiO}_x/\text{C}$ -673. As noted, the pore of sample $\text{Fe}_2\text{O}_3@\text{TiO}_x/\text{C}$ -673 was mainly distributed in narrow range of 1.7–6.0 nm, but $\text{Fe}_2\text{O}_3@\text{SiO}_x/\text{C}$ held a wide pore size distribution located between 1.8 and 20.0 nm (Fig. 4b and c). Combining the BJH pore size distribution with SEM

images, we consider that the prepared $\text{MO}_x(\text{M}=\text{Ti}, \text{Si})/\text{C}$ microellipsoids possess a hierarchical network surface structure at macro-, meso-, and microscale. Hence, it is suggested that such high surface area and porosity of the pollen-templated replicas can favourably provide a confined micro-environment for stabilization of highly disperse metal oxide and have potential applications in heterogeneous catalysis [23].

In order to more clearly reveal the porous microstructures of hollow porous MO_x/C microellipsoids and the supported NPs, TEM and HRTEM were carried out (Fig. 5). As apparent from images, it is found that the titanium and silicon coating layer is uniformly distributed on the external surface of carbon matrix (Fig. 5a and b). The outside edge of sample hollow porous SiO_x/C exhibits the unique porous structure, which consists of the regularly-dispersed circular hole with the diameter of about 10 nm (blue rectangle area). Fig. 5c and d shows the TEM images of TiO_x/C -873 and SiO_x/C -873. An intriguing multi-level hierarchically porous microstructure can be observed for the prepared TiO_2 and SiO_2 . After decorated with Fe_2O_3 , it is clear that the ultrafine nanocrystals have been encapsulated into the pore of amorphous MO_x/C hybrid composites (Fig. 5e and f). In comparison, in situ grown NPs have been homogeneously dispersed throughout porous silica/carbon matrix with the mean size of 1.60 nm, much smaller than that in sample $\text{Fe}_2\text{O}_3@\text{hollow porous TiO}_x/\text{C}$ (2.40 nm). Moreover, HRTEM images also confirm that Fe_2O_3 NPs are in good dispersion inside the frameworks of composites (Fig. 5g and h), and the lattice spacing of supported NPs for sample $\text{Fe}_2\text{O}_3@\text{TiO}_x/\text{C}$ -673 (g) and $\text{Fe}_2\text{O}_3@\text{SiO}_x/\text{C}$ -673 is 0.25 nm belonging to the spacing of the (110) plane of $\alpha\text{-Fe}_2\text{O}_3$ crystal [24].

The crystal phases of various Ti-based and Si-based supported microellipsoids at different calcination temperatures were analyzed by XRD, the resulted patterns are presented in Fig. 6a and b. It is clear that only a wide diffraction peak around 18.5° appears which shows the amorphous components in pollen grains [25,26]. After sol-gel coating and calcined at 473 K, an obvious reduction in the intensity of pollen characteristic peak was observed, which could be due to the growth and crystallization of coating inorganic substance [20,27]. It suggests successful coating of Ti and Si precursors on the surface of carbon matrix. When the calcination temperature increased to 673 K, it was worthy to note that a shift to the higher diffraction angle for pollen characteristic peak and

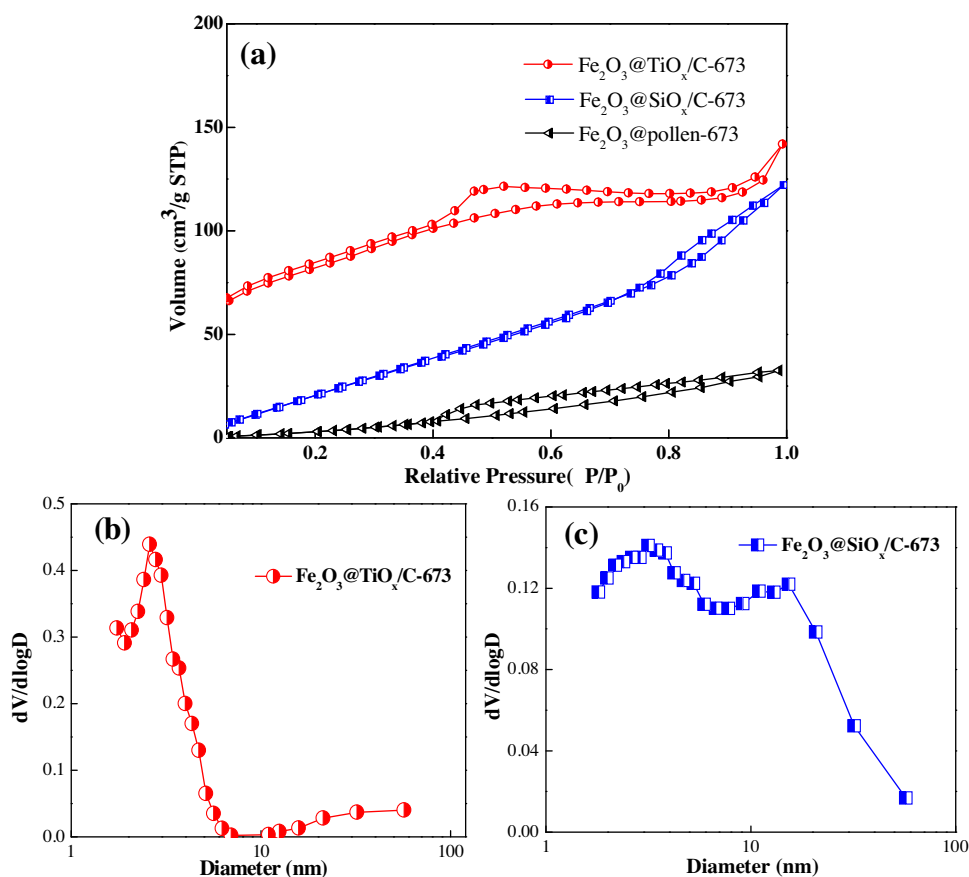


Fig. 4. Nitrogen adsorption/desorption isotherms and pore size distribution for the prepared microellipsoids.

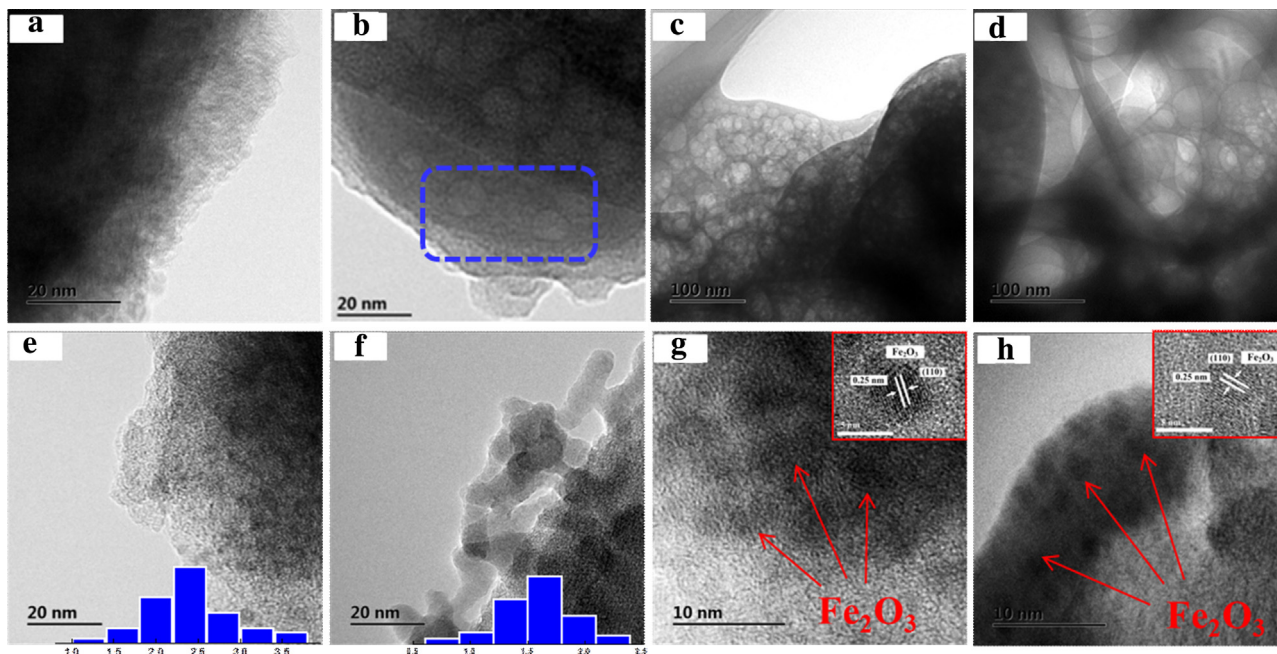


Fig. 5. TEM images of sample $\text{TiO}_x/\text{C}-673$ (a), $\text{SiO}_x/\text{C}-673$ (b), $\text{TiO}_x/\text{C}-873$ (c), $\text{SiO}_x/\text{C}-873$ (d), $\text{Fe}_2\text{O}_3@/\text{TiO}_x/\text{C}-673$ (e) and $\text{Fe}_2\text{O}_3@/\text{SiO}_x/\text{C}-673$ (f); HRTEM images of sample $\text{Fe}_2\text{O}_3@/\text{TiO}_x/\text{C}-673$ (g) and $\text{Fe}_2\text{O}_3@/\text{SiO}_x/\text{C}-673$ (h). The inset is HRTEM image of lattices of Fe_2O_3 .

no typical diffraction peaks belonging to the separate MO_x were observed in the composites. The shift could be ascribed to the chemical interaction between the substituted or incorporated inorganic species and carbon [28,29]. After the precursors were annealed

in a flowing air at 873 K, the diffraction pattern of TiO_x/C can be indexed to standard peaks of anatase TiO_2 (JCPDS 21-1272). It was found that $\text{SiO}_x/\text{C}-873$ presented a broad characteristic peak at 2θ of $25\text{--}28^\circ$ corresponding to the amorphous silica. Meanwhile, two

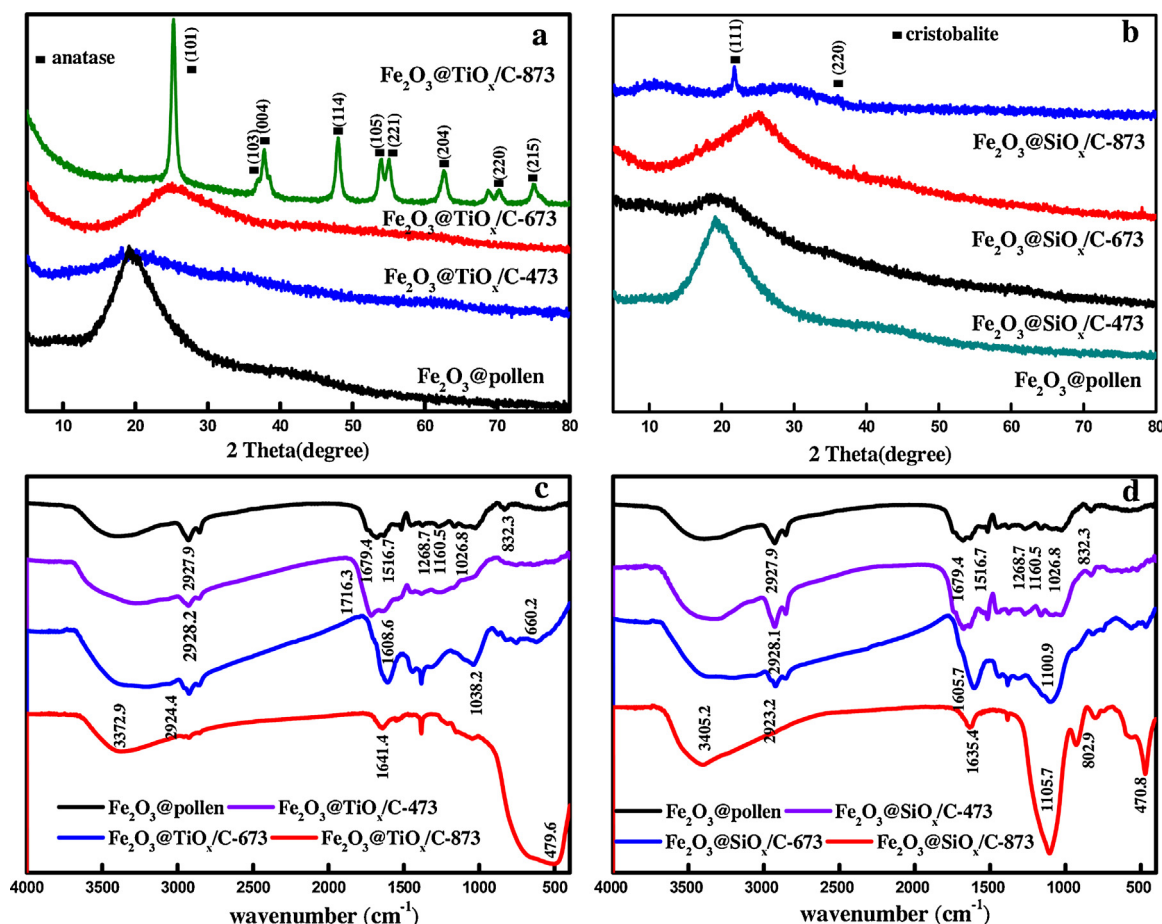


Fig. 6. XRD patterns of Fe_2O_3 @pollen, Fe_2O_3 @ TiO_x/C composites (a) and Fe_2O_3 @ SiO_x/C composites (b); FTIR spectra of Fe_2O_3 @pollen, Fe_2O_3 @ TiO_x/C composites (c) and Fe_2O_3 @ SiO_x/C composites (d).

small peaks at 2θ of 21.7 and 35.9° were shown and reflected from the planes (111) and (220) of cristobalite SiO_2 (JCPDS 270605), so it could be considered as semi-crystallized. These results demonstrated that the calcination temperature had a significant effect on the crystal form of composites. Moreover, no obvious diffraction peaks of ferric oxide were found, which indicated the formation of small particles inside the frameworks of hybrid materials.

Fig. 6c and d record the FTIR spectra of different composites. From the curve of pollen grains, the absorption peaks around 2927.9 cm^{-1} are assigned to the stretching vibration of methylene groups. The band of 1026.8 and 1679.4 cm^{-1} can be attributed to C–N stretching of protein and bending vibration of –NH group, respectively [30]. The carboxylate –COO– stretching bands of biomacromolecules (such as aliphatic acid) at 1268.7 cm^{-1} for symmetric vibration and C=C stretching at 1516.7 cm^{-1} are also obtained [23]. After coating and post-treatment, the variation on the surface property and function of Ti- and Si-based composites was evidenced by the FTIR data. When calcined at 473 K, no obvious change of absorption peaks was observed in the spectrum of SiO_x/C -473 compared with pure pollen, however, a decrease in the intensity of some pollen absorption peaks (such as 1160.5, 1026.8 and 832.3 cm^{-1}) was presented for sample TiO_x/C -473. The result indicated that the introduction of Ti had a more obvious effect on the functional group of carbon matrix than Si species under the low temperature heat-treatment. As the calcination temperature increased to 673 K, it was evident that most of characteristic peaks intensities for pollen grains decreased and a few absorption peaks (1516.7 cm^{-1}) disappeared, whereas the Si–O asymmetric stretching vibration at 1100.9 cm^{-1} appeared in the spectrum of

SiO_x/C -673 [31]. For sample TiO_x/C -673, an evident increase in the intensity of peak at 1038.2 cm^{-1} belonging to the stretching vibration of C–O was shown and a new broad Ti–O vibration band at 660.2 appeared [32]. This highlighted the fact that the decomposition and oxidation of carbon frameworks began to occur and the generated inorganic oxides were dispersed on the surface of carbon matrix after calcined at 673 K. In the curve of MO_x/C -873, the stretching vibration of –CH disappeared, and a remarkable increase in intensity of characteristic Ti–O and Si–O peaks was observed. Compared with other samples, a stronger absorption peak around 3400 cm^{-1} was obtained for TiO_x/C -873 and SiO_x/C -873, which implied that more dissociative hydroxyl groups were adsorbed on the surface [24].

To confirm the surface chemical state of composite microellipsoids, the XPS was conducted. In full XPS spectra of Fe_2O_3 @ TiO_x/C -673, Fe_2O_3 @ SiO_x/C -673 and Fe_2O_3 @pollen-673, the presence of O1s, C1s, Si2p, Ti2p, and Fe2p can be presented (Fig. 7a). As depicted in Fig. 7b, C 1s spectra of the samples are resolved into 284.7 eV (C–C) and 286.1 eV (C–O) [33,34]. Compared with Fe_2O_3 @pollen-673, a slight shift (0.4–0.5 eV) to lower binding energy of C 1s for C–O bond suggests a change of chemical environment due to introduction of inorganic species, in agreement with XRD analysis. In the fitting curve (Fig. 7c), the binding energy of Fe 2p for sample Fe_2O_3 @ SiO_x/C -673 are 713.4 and 727.1 eV, which are assigned to spectra of Fe 2p_{3/2} and Fe 2p_{1/2} for the lattice Fe^{III} -O in Fe_2O_3 , respectively [35]. Compared with Fe_2O_3 @ TiO_x/C -673 and Fe_2O_3 @pollen-673, a higher binding energy can be observed for sample Fe_2O_3 @ SiO_x/C -673, which indicates that the electron density of Fe 2p decreases with the introduction of Si species. This

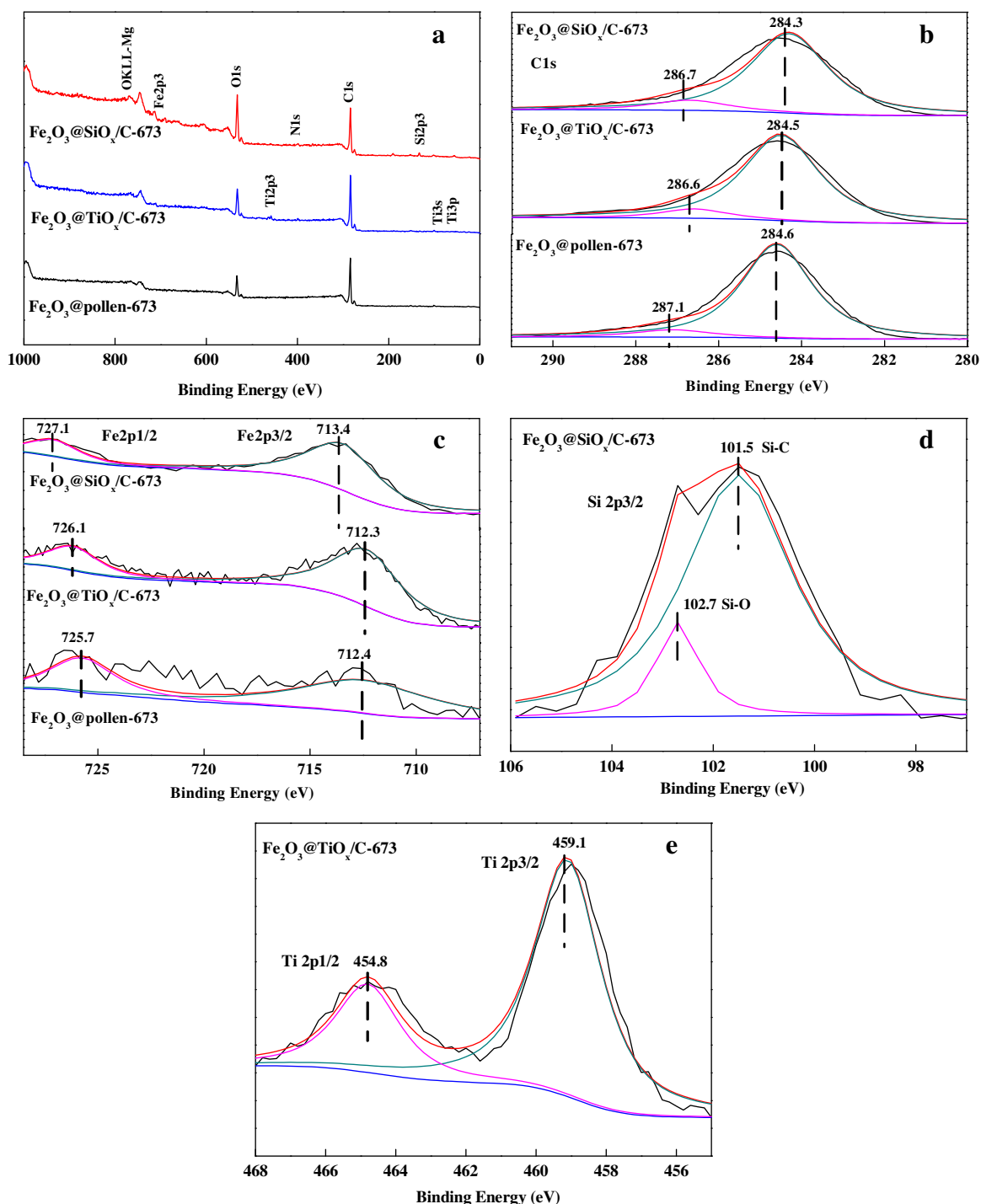


Fig. 7. XPS spectra of the different samples: (a) full spectra and fine XPS spectra of (b) C 1s, (c) Fe 2p, (d) Si 2p3/2, and (e) Ti 2p.

shift can be ascribed to the formation of Si–O–Fe bond in the crystal lattice and the electronegativity of Si higher than Ti and Fe [36]. Moreover, the binding energy of the Ti 2p for sample is observed at 459.1 and 464.8 eV, which are contributed to the Ti 2p2/3 and Ti 2p1/2 of $\text{Ti}^{\text{IV}}\text{-O}$ species (Fig. 7e). The separation between the two peaks is 5.7 eV, which confirms the presence of Ti^{4+} species in the composites. As shown in Fig. 7d, the spectrum of Si 2p can be resolved into two contributions for $\text{Fe}_2\text{O}_3/\text{SiO}_x/\text{C-673}$, the main band of Si 2p s at 102.7 eV is assigned to the Si–O species, and the contribution at around 101.5 eV belongs to the Si–C groups [37].

3.2. Effect of structure and property of support on catalytic activity

The performance of the prepared microellipsoids was evaluated by photo-Fenton oxidation of organic contaminants under visible-light irradiation [38]. In order to better address the advantage of the hierarchically porous structure and filled carbon layer of pollen-templated MiO_x/C , the conventional supports such as active carbon (AC), P25 and SiO_2 were also tested. Fig. 8a–c shows the catalytic oxidation efficiency by using different catalysts. A control experiment showed that the X-3B was stable in

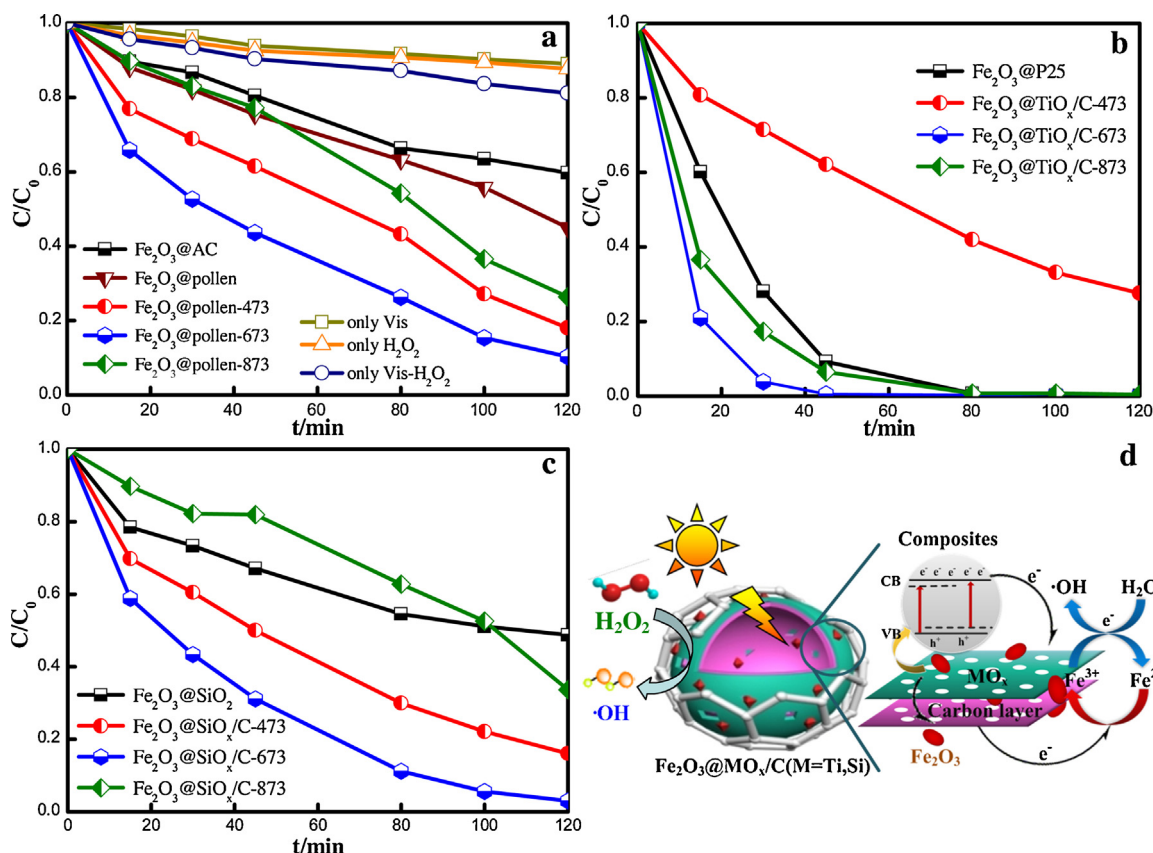


Fig. 8. (a–c) Photocatalytic oxidation of X-3B as function of time in the presence of different prepared catalysts. ($T = 298 \text{ K}$, $C_{\text{cat}} = 0.2 \text{ g L}^{-1}$, $C_{\text{X-3B}} = 100 \text{ mg L}^{-1}$, $C_{\text{H}_2\text{O}_2} = 9.8 \text{ mmol L}^{-1}$, $\text{pH} = 5.0$). (d) Schematic diagram of Fe_2O_3 @ MO_x ($M = \text{Ti, Si}$)/Carbon for photocatalytic oxidation.

the presence of visible light irradiation and/or H_2O_2 , which indicated that the decolorization of dyes did not proceed without the catalysts. For comparison, the effect of calcination temperature on catalytic activity of the Fe_2O_3 @pollen carbon was highlighted. It was evident that an obvious increase in the degradation efficiency and kinetic rate constant was obtained along with the increase of temperature, however, further increase of the calcination temperature led to a significant decrease of photocatalytic activity since Fe_2O_3 @pollen-873 ($k = 0.0086 \text{ min}^{-1}$) showed lower activity than Fe_2O_3 @pollen-673 ($k = 0.0195 \text{ min}^{-1}$) (Table S3 ESI[†], fitted by pseudo first-order kinetics model). Like Fe_2O_3 @pollen carbon, the photocatalysts Fe_2O_3 @ TiO_x /C and Fe_2O_3 @ SiO_x /C showed the same activity trend. Among various samples, it was found that the kinetic rate constants of Fe_2O_3 @ TiO_x /C-673 ($k = 0.1050 \text{ min}^{-1}$) and Fe_2O_3 @ SiO_x /C-673 ($k = 0.0286 \text{ min}^{-1}$) exhibited 1.5–5.0 times higher activity than that of Fe_2O_3 @pollen-673, indicating that the introduction of Ti and Si species into carbon structure had a positive effect on the decomposition of hydrogen peroxide to hydroxyl radical ($\cdot\text{OH}$) radical. As noted, sample Fe_2O_3 @ TiO_x /C-673 showed the best performance and the rate constant was also higher than that of Fe_2O_3 @ SiO_x /C-673. Referring to the above characterizations, the enhanced performance on degradation of X-3B over Fe_2O_3 @ TiO_x /C-673 and Fe_2O_3 @ SiO_x /C-673 could be ascribed to the characteristics of surface functional groups and structure of support. As reported, the surface functional group of support (especially carboxyl, amine and hydroxyl group) can enhance the interfacial interaction between the carbon and metal sites, and consequently improve the dispersion of active species on composites matrix [39,40]. Meanwhile, the oxygen of the functional group could promote photo-induced electron transfer between active sites and carbon atoms [39]. Besides surface properties, large

surface area and high pore volume are benefit for adsorbing enough active sites and reactant, and thus promote photocatalytic reactions. Compared with Fe_2O_3 @ SiO_x /C-673, the superior activity of Fe_2O_3 @ TiO_x /C-673 was mainly accredited to the larger surface area, higher pore volume and the introduction of TiO_2 photocatalytic sites. More importantly, the advancement of the structure and properties led to several-fold enhancement of photocatalytic efficiency for fabricated composite microellipsoids compared with conventional AC ($k = 0.0047 \text{ min}^{-1}$), P25 ($k = 0.0419 \text{ min}^{-1}$) and SiO_2 supported photocatalysts ($k = 0.0073 \text{ min}^{-1}$). The characterization results of sample Fe_2O_3 @AC, Fe_2O_3 @P25 and Fe_2O_3 @ SiO_2 were presented in the supporting information (Fig. S3–6 ESI[†]).

Fig. 8d provides proposed mechanism related to the synergistic interfacial effect of Fe_2O_3 NPs and carbon-based composites. Hollow and hierarchically porous structure of the support can obviously improve the light utilization efficiency, as some of the photons enter the porous structure and are absorbed by the inorganic compound and Fe_2O_3 NPs. Subsequently, the heterostructure of Fe_2O_3 / MO_x -C composites had a wider range of light absorption. Fig. S7 shows the UV–vis diffuse reflectance spectra (DRS) of the samples. Compared with P25 and SiO_2 support, the active carbon layer can enhance light absorption intensity and further extend the range of light absorption wavelength. Moreover, the carbon species could narrow the band gap of semiconductor and promote the transportation and separation of photogenerated electrons to accelerate Fe^{III} converting to Fe^{II} owing to the excellent conductivity of composites [41–43]. The generated Fe^{II} species will continue to react with H_2O_2 to produce the $\cdot\text{OH}$ and Fe^{III} on the surface of microellipsoids. Compared with the conventional supports, the conversion efficiency of the $\text{Fe}^{\text{II}}/\text{Fe}^{\text{III}}$ cycle reaction occurring on the carbon based composites was much higher due to the high

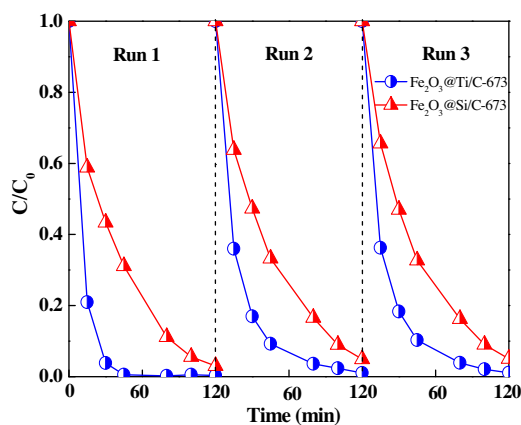


Fig. 9. Reusability of the Fe_2O_3 @hollow porous $\text{TiO}_x/\text{C}-673$ and Fe_2O_3 @hollow porous $\text{SiO}_x/\text{C}-673$ microellipsoids after subsequent reactions.

concentration of electrons on their multifunctional layer. In this regard, it is reasonable to believe that the superior catalytic properties of Fe_2O_3 @ $\text{TiO}_x/\text{C}-673$ are derived from the strong interaction between the carbon groups and TiO_2 and Fe_2O_3 . Due to conduction band of Fe_2O_3 more positive than that of TiO_2 , Fe_2O_3 supported on the surface of TiO_2 made it possible for the photogenerated electrons to migrate from TiO_2 to Fe^{III} and further converted to Fe^{II} , which made significant contributions toward decomposition of H_2O_2 to hydroxyl radical [35]. Moreover, the carbon layer further facilitated the movement of the excited electrons from TiO_2 to Fe_2O_3 particles under visible light irradiation [44,45]. Meanwhile, photo-induced holes accumulated in valence band of TiO_2 could be favorable for splitting of H_2O to hydroxyl radicals. With regard to the best photocatalyst of Fe_2O_3 @ $\text{TiO}_x/\text{C}-673$ microellipsoids, it has a very stable activity toward the dye degradation as the leaching content of Fe ions remained below 0.01 mg L^{-1} , much lower than that for Fe_2O_3 @P25 (Fig. S8 ESI†). This reveals that the hierarchically porous and hollow structure of biotemplated composites plays an important role on the stabilization of ultrafine NPs well dispersed.

3.3. Catalyst stability

The stability and reusability of prepared microellipsoids were evaluated by the recycling tests. The catalysts were recovered by the washing and thermal treatment. As illustrated by Fig. 9, no obvious loss of catalytic activity was presented in three consecutive cycles, because more than 95.0% photobleaching was observed under the same condition for all runs. The content of leached Fe^{3+} during the catalytic oxidation kept below 0.2 mg L^{-1} in three cycles. Meanwhile, TEM images pointed out the framework structure of MO_x/C ellipsoids was not destroyed after catalytic oxidation (Fig. S9 ESI†). The result well demonstrated that the incorporation of inorganic compounds can greatly enhance the stability of carbon material in catalytic oxidation.

4. Conclusions

In summary, we put forward a bioinspired sol-gel coating method to fabricate novel hollow and hierarchically porous $\text{MO}_x(\text{M}=\text{Ti}, \text{Si})/\text{carbon}$ microellipsoids supported with Fe_2O_3 . By this strategy, very active and reusable catalysts can be obtained for visible-light assisted photooxidation at neutral pH due to the hollow and hierarchically porous structure of biotemplated composite ellipsoids with high surface area and wide pore size distribution. High-level control of artificial carbon-based composites with structure and function can lead the prepared catalysts to present much

higher performance than that of activated carbon, TiO_2 and SiO_2 supported materials. Moreover, the strong interaction between the carbon source and TiO_2 semiconductor made Fe_2O_3 @ $\text{TiO}_x/\text{C}-673$ exhibit superior catalytic properties by accelerating the movement of excited charges. As the bioinspired hollow and hierarchically porous structure can provide a high surface area and multiple pore size distribution for NPs to homogeneously disperse on the wall of carbon-based composites, the approach can be applied more generally to various biomaterials.

Acknowledgements

We thank for financial support the National Natural Science Foundation of China (Grant Nos. 21236008, 21506193 and 21476206), the Fujian Provincial Department of Ocean (Grant No.2014-06), Taishan Scholarship Blue Industry Program from Shandong Provincial Government (Grant No. 2014008) and the Minjiang Scholarship from Fujian Provincial Government, Zhejiang Provincial Bureau of Science and Technology (Grant No. 2016C33007), China Postdoctoral Science Foundation (Grant No. 2015M581958), and the Zhejiang Provincial Postdoctoral Science Foundation.

Appendix A. Supplementary data

Supplementary data associated with this article can be found, in the online version, at <http://dx.doi.org/10.1016/j.apcatb.2016.04.051>.

References

- [1] Z. Yang, J. Ren, Z. Zhang, X. Chen, G. Guan, L. Qiu, Y. Zhang, H. Peng, *Chem. Rev.* 115 (2015) 5159–5223.
- [2] N.A. Zubir, C. Yacou, J. Motuzas, X. Zhang, X.S. Zhao, J.C.D. da Costa, *Chem. Commun.* 51 (2015) 9291–9293.
- [3] S. Guo, G. Zhang, Y. Guo, J.C. Yu, *Carbon* 60 (2013) 437–444.
- [4] B. Qiu, Q. Li, B. Shen, M. Xing, J. Zhang, *Appl. Catal. B* 183 (2016) 216–223.
- [5] D. Eder, *Chem. Rev.* 110 (2010) 1348–1385.
- [6] I. Inoue, H. Yamauchi, N. Okamoto, K. Toyoda, M. Horita, Y. Ishikawa, H. Yasueda, Y. Uraoka, I. Yamashita, *Nanotechnology* 26 (2015) 285601.
- [7] Y. Zhang, Z.R. Tang, X. Fu, Y.J. Xu, *ACS Nano* 4 (2010) 7303–7314.
- [8] H. Sai, K.W. Tan, K. Hur, E. Asenath-Smith, R. Hovden, Y. Jiang, M. Riccio, D.A. Muller, V. Elser, L.A. Estroff, S.M. Gruner, U. Wiesner, *Science* 341 (2013) 530–534.
- [9] W.L. Noorduin, A. Grinthal, L. Mahadevan, J. Aizenberg, *Science* 340 (2013) 832–837.
- [10] D. Wang, T. Hisatomi, T. Takata, C. Pan, M. Katayama, J. Kubota, K. Domen, *Angew. Chem. Int. Ed.* 52 (2013) 11252–11256.
- [11] Q.G. Shao, J. Tang, Y.X. Lin, F.F. Zhang, J.S. Yuan, H. Zhang, N. Shinya, L.C. Qin, *J. Mater. Chem. A* 1 (2013) 15423–15428.
- [12] P. Guo, H. Song, X. Chen, *J. Mater. Chem.* 20 (2010) 4867–4874.
- [13] H. Zhou, X. Li, T. Fan, F.E. Osterloh, J. Ding, E.M. Sabio, D. Zhang, Q. Guo, *Adv. Mater.* 22 (2010) 951–956.
- [14] C. Yin, S.M. Zhu, Z.X. Chen, W. Zhang, J.J. Gu, D. Zhang, *J. Mater. Chem. A* 1 (2013) 8367–8378.
- [15] X. Dang, H. Yi, M.H. Ham, J. Qi, D. Soo Yun, R. Ladewski, M.S. Strano, P.T. Hammond, A.M. Belcher, *Nature Nanotech.* 6 (2011) 377–384.
- [16] Y. Zhao, M. Wei, J. Lu, Z.L. Wang, X. Duan, *ACS Nano* 3 (2009) 4009–4016.
- [17] Z. Zhou, G.J. Bedwell, R. Li, P.E. Prevelige, A. Gupta, *Sci. Rep.* 4 (2014) 3832.
- [18] S.R. Hall, H. Bolger, S. Mann, *Chem. Commun.* (2003) 2784–2785.
- [19] S.R. Hall, V.M. Swinerd, F.N. Newby, A.M. Collins, S. Mann, *Chem. Mater.* 18 (2006) 598–600.
- [20] Y. Xia, W. Zhang, Z. Xiao, H. Huang, H. Zeng, X. Chen, F. Chen, Y. Gan, X. Tao, *J. Mater. Chem.* 22 (2012) 9209–9215.
- [21] W.B. Goodwin, I.J. Gomez, Y. Fang, J.C. Meredith, K.H. Sandhage, *Chem. Mater.* 25 (2013) 4529–4536.
- [22] S. Bose, T. Kuila, M.E. Uddin, N.H. Kim, A.K.T. Lau, J.H. Lee, *Polymer* 51 (2010) 5921–5928.
- [23] L. Qin, Z.W. Li, Z. Xu, X. Guo, G. Zhang, *Appl. Catal. B* 179 (2015) 500–508.
- [24] G. Zhang, L. Qin, Y. Wu, Z. Xu, X. Guo, *Nanoscale* 7 (2015) 1102–1109.
- [25] F. Cao, D.X. Li, *Bioinspir. Biomim.* 5 (2010) 016005.
- [26] Y. Wang, Z.M. Liu, B.X. Han, Y. Huang, G. Yang, *Langmuir* 21 (2005) 10846–10849.
- [27] W. Tu, Y. Zhou, Q. Liu, Z. Tian, J. Gao, X. Chen, H. Zhang, J. Liu, Z. Zou, *Adv. Funct. Mater.* 22 (2012) 1215–1221.

- [28] L. Qin, G. Zhang, Z. Fan, Y. Wu, X. Guo, M. Liu, *Chem. Eng. J.* 244 (2014) 296–306.
- [29] Z. Li, Y. Wang, J. Liu, G. Chen, Y. Li, C. Zhou, *Int. J. Hydrogen Energy* 34 (2009) 147–152.
- [30] A. Ata, O.O. Nalcaci, B. Ovez, *Algal Res.* 1 (2012) 194–204.
- [31] P. Xu, J. Lu, T. Xu, S. Gao, B. Huang, Y. Dai, *J. Phys. Chem. C* 114 (2010) 9510–9517.
- [32] V. Umamaheswari, M. Palanichamy, V. Murugesan, *J. Catal.* 210 (2002) 367–374.
- [33] Q. Liu, Y. Guo, Z. Chen, Z. Zhang, X. Fang, *Appl. Catal. B* 183 (2016) 231–241.
- [34] H. Yin, S. Zhao, J. Wan, H. Tang, L. Chang, L. He, H. Zhao, Y. Gao, Z. Tang, *Adv. Mater.* 25 (2013) 6270–6276.
- [35] L. Qin, X. Pan, L. Wang, X. Sun, G. Zhang, X. Guo, *Appl. Catal. B* 150–151 (2014) 544–553.
- [36] R.T. Sander son, *Chemical Bonds and Bond Energy*, 2nd ed., Academic Press, New York, 1976, pp. 40–42, 67–68.
- [37] Y. Yang, J. Lan, X. Li, *Mater. Sci. Eng. A* 380 (2004) 378–383.
- [38] Y. Gao, Y. Wanga, H. Zhang, *Appl. Catal. B* 178 (2015) 29–36.
- [39] M. Park, B.H. Kim, S. Kim, D.S. Han, G. Kim, K.R. Lee, *Carbon* 49 (2011) 811–818.
- [40] K.-H. Chuang, C.-Y. Lu, M.-Y. Wey, Y.-N. Huang, *Appl. Catal. A* 397 (2011) 234–240.
- [41] X. Yu, J. Liu, Y. Yu, S. Zuo, B. Li, *Carbon* 68 (2014) 718–724.
- [42] Y. Zhang, Z.R. Tang, X. Fu, Y.J. Xu, *ACS Nano* 5 (2011) 7426–7435.
- [43] Y. Shao, C. Cao, S. Chen, M. He, J. Fang, J. Chen, X. Li, D. Li, *Appl. Catal. B* 179 (2015) 344–351.
- [44] L. Zhao, X. Chen, X. Wang, Y. Zhang, W. Wei, Y. Sun, M. Antonietti, M.-M. Titirici, *Adv. Mater.* 22 (2010) 3317–3321.
- [45] K. Gutbrod, P. Greil, C. Zollfrank, *Appl. Catal. B* 103 (2011) 240–245.